(Received 31 March 2026, Accepted 12 May 2026, Scheduled 22 June 2026)

Thermal and Power Stress Equivalence Between Stratospheric Balloon and Low Earth Orbit Environments for CubeSat Subsystem Screening

Aryan Takalkar[1], Raj Devalkar[1], Shubhangi Kharche[1,*], and Kondaka LakshmiSudha[2]

[1] *Department of Electronics and Computer Science Engineering, SIES Graduate School of Technology, Navi Mumbai, India*
[2] *Department of Information Technology, SIES Graduate School of Technology, Navi Mumbai, India*

ABSTRACT: CubeSats deployed into Low-Earth Orbit (LEO) are continuously subjected to cyclic thermal loads and power-system degradation. Replicating these stresses through traditional space qualification is resource-intensive, placing it beyond the reach of most academic teams. Stratospheric High-Altitude Balloon (HAB) platforms offer a cost-effective pre-qualification pathway; however, no previous work has provided a rigorous, analytical method for mapping the stress accumulated during a balloon flight to an equivalent fraction of LEO stress. This gap prevents defensible claims of environmental fidelity. This paper introduces the High Altitude to Low Earth Orbit Correlation Index – Thermal and Power (HLCI-TP), a physics-based composite metric comprising three independently computed sub-indices: thermal fatigue (Coffin-Manson model), electrochemical battery degradation (Arrhenius model), and Ultraviolet (UV) fluence (Beer-Lambert model). Each sub-index quantifies the fraction of a 30-day LEO reference stress budget reproduced during a balloon mission, and the three are combined via a weighted linear sum. The UV sub-index is grounded in the Beer-Lambert electromagnetic attenuation law, directly connecting the framework to the quantification of solar ultraviolet irradiance — a component of the electromagnetic spectrum — at stratospheric altitudes. For a 24-hour reference mission at 35 km, the computed sub-index values are $R_T \approx 1.63 \times 10^{-4}$ (thermal), $R_P \approx 2.0 \times 10^{-6}$ (electrochemical), and $R_U \approx 9.92 \times 10^{-3}$ (UV), yielding a composite HLCI-TP score of 2.07×10^{-3}, which falls within the "minimal screening" band. This result is robust across three distinct weighting configurations (factor-of-three spread), a 10,000-sample Monte Carlo uncertainty analysis, and across the full practical range of mission durations (6–48 hours). The framework is further corroborated by applying Rainflow cycle counting to real GPS altitude data from the PMC-Turbo stratospheric balloon mission (35.7–39.5 km, 134.8 hours), which confirms the minimal-screening classification across all tested durations. These results quantify, for the first time through an analytical framework, that a 24-hour stratospheric flight reproduces approximately 0.016% of the LEO thermal fatigue budget and approximately 1% of the LEO UV-A/UV-B fluence budget. The cost savings relative to full Thermal Vacuum Chamber (TVAC) testing are one to two orders of magnitude. Future work will target orbital calibration, a vibration sub-index, and an open-source web calculator.

1. INTRODUCTION

Over the last 20 years, the rapid democratization of space has changed how we access orbital platforms. The 1U CubeSat standard, first formally proposed by Heidt et al. [1] and operationalized through the development of the Poly-Picosatellite Orbital Deployer (P-POD) by Puig-Suari et al. [2], established a 10 cm cubic form factor and a common deployer interface that dramatically lowered the barrier to orbit for academic and small commercial teams. Reduced launch costs and an increasing number of satellites being launched by universities have further broadened access to orbital platforms [5, 6]. Statistical surveys of the first hundred CubeSat missions confirm that, while launch rates have accelerated, on-orbit success rates have remained variable, with subsystem failures constituting a primary cause of anomalies [3]. This growth in small-satellite activity has not been matched by an equivalent improvement in subsystem qualification methods [7, 8]. The growing variety of CubeSat and microsatellite mission concepts, including propulsion-enabled constellation reconfigurations [4], further underscores the need for cost-effective, standardized qualification pathways that scale across diverse mission profiles.

Environmental testing is among the most critical subsystem qualification processes, as it demonstrates that a satellite will withstand the combined thermal, vacuum, and radiation stresses encountered in LEO. Unfortunately, environmental testing is resource-intensive, and most university teams are constrained in their ability to conduct such tests [6]. As a result, many academic missions are launched without adequate exposure to representative environmental conditions, creating a persistent disconnect between design assumptions and in-orbit reliability. This disconnect is not merely procedural; subsystem-level deficiencies continue to account for a significant fraction of mission anomalies [7, 8].

University teams also lack accessible, standardised frameworks for mapping their test exposures onto LEO-relevant stress budgets [6, 9]. CubeSat subsystem verification is typi-

* Corresponding author: Shubhangi Kharche (shubhangi.kharche@gmail.com).

NOMENCLATURE

Abbreviations

AM0	Air Mass Zero (extraterrestrial solar irradiance spectrum)
CTE	Coefficient of Thermal Expansion
DoF	Degrees of Freedom
EPS	Electrical Power System
GEVS	General Environmental Verification Standard
GNSS	Global Navigation Satellite System
HAB	High-Altitude Balloon
HLCI-TP	High Altitude to Low Earth Orbit Correlation Index – Thermal and Power
IMU	Inertial Measurement Unit
LEO	Low Earth Orbit
Li-poly	Lithium Polymer
LoRa	Long Range (radio modulation technology)
MEMS	Micro-Electro-Mechanical Systems
NASA	National Aeronautics and Space Administration
OBC	Onboard Computer
P-POD	Poly-Picosatellite Orbital Deployer
PMC	Polar Mesospheric Cloud
PSD	Power Spectral Density
RTD	Resistance Temperature Detector
TVAC	Thermal Vacuum Chamber
UART	Universal Asynchronous Receiver-Transmitter
UV	Ultraviolet
UV-A	Ultraviolet A (315–400 nm)
UV-B	Ultraviolet B (280–315 nm)
UV-C	Ultraviolet C (100–280 nm)
VUV	Vacuum Ultraviolet (<200 nm)
WMO	World Meteorological Organization

Mathematical and Physical Symbols

Symbol	*Description*	*Units*
α	Effective CTE mismatch between bonded materials	[°C^{-1}]
$\Delta\varepsilon_p$	Plastic strain range	[–]
ΔT	Peak-to-peak temperature excursion	[°C]
ξ	Daylight fraction	[–]
$\tau(z,\lambda)$	Atmospheric optical depth above altitude z	[–]
λ	Wavelength	[nm]
AF	Arrhenius acceleration factor	[–]
C	Coffin–Manson material constant	[–]
D, D_{HAB}, D_{LEO}	Cumulative thermal damage (total / HAB / LEO)	[–]
E_a	Activation energy	[eV]
f_{HAB}	UV fraction of AM0 at balloon altitude	[–]
F_{HAB}, $F_{\mathrm{LEO,ref}}$	Accumulated UV fluence (HAB / LEO ref.)	[W h m^{-2}]
$I_0(\lambda)$	AM0 solar spectral irradiance	[W m^{-2} nm^{-1}]
$I(z,\lambda)$	Solar irradiance at altitude z	[W m^{-2} nm^{-1}]
k_B	Boltzmann constant (8.617×10^{-5} eV K^{-1})	[eV K^{-1}]
m	Coffin–Manson fatigue ductility exponent	[–]
N_f, N_{HAB}, N_{LEO}	Thermal cycles (to failure / HAB / LEO ref.)	[cycles]
R_T, R_P, R_U	Sub-indices: thermal / power / UV	[–]
t_{eq}	Equivalent aging time at T_{ref}	[hr]
t_{flight}, t_{HAB}	HAB float / total mission duration	[hr]
$t_{\mathrm{LEO,ref}}$	LEO reference mission duration (720 hr)	[hr]
T_{ref}, T_{test}	Arrhenius reference / test temperature	[K]
w_T, w_P, w_U	Sub-index weighting factors	[–]

cally referenced to acceptance criteria, such as the NASA General Environmental Verification Standard (GEVS) [10], which prescribes thermal/vacuum cycling, vibration, and radiation tests whose costs frequently exceed academic mission budgets [5]. Consequently, much CubeSat hardware is tested only under ambient or partially representative conditions, leaving critical thermal fatigue and environmental degradation failure modes undetected prior to launch [7–9].

High-Altitude Balloon (HAB) platforms operate within the stratosphere (30–40 km altitude), exposing payloads to reduced pressure, elevated UV radiation, and dynamic thermal conditions that share qualitative features with aspects of LEO. Prior work has demonstrated HAB utility for early-stage validation, including testing communication links [11] and evaluating remote sensing payloads [12]. Thermal and dynamic characteristics of balloon-borne systems have been measured and shown to constitute a near-space analog [13, 14], and balloon platforms have been proposed as low-cost pre-qualification vehicles for space hardware. However, stratospheric conditions are frequently described as "space-representative" without rigorous quantification of the fraction of orbital stress actually reproduced [12]. This absence of a quantitative mapping substantially limits the defensibility and comparability of HAB-based test results.

The lack of a standardised stress-equivalence metric is a significant gap in the literature. Reliability studies consistently identify inadequate environmental testing as a major contributor to mission failure [7, 8], yet provide no practical basis for connecting accessible suborbital test environments to orbital stress conditions. Existing HAB campaigns yield useful environmental measurements but do not support a defensible estimate of their LEO stress equivalence, creating both direct impacts (undetected subsystem failures) and indirect impacts (unwarranted confidence in pre-flight test results) [8].

This paper addresses this gap through two contributions. First, it formalises the role of HAB platforms in the CubeSat development process by introducing a quantifiable stress-equivalence framework. Second, it moves beyond descriptive environmental comparisons to define measurable equivalences, integrating multiple environmental parameters into a unified composite stress metric — an integration not previously achieved in the open literature [6, 9]. The UV fluence sub-index is derived from the Beer-Lambert electromagnetic attenuation law, connecting the framework to the broader scope of solar UV irradiance quantification as an electromagnetic phenomenon.

TABLE 1. Pressure and convective heat transfer across reference environments.

Environment	Pressure	Convective HT
Sea Level	∼101,300 Pa	Strong
HAB (∼35 km)	∼50 Pa	Very weak
LEO (∼400 km)	$< 10^{-7}$ Pa	None

The framework is not intended to replace high-fidelity qualification techniques; rather, it provides a calibrated, transparent intermediate step that enables the early identification of validation gaps and supports better resource allocation decisions.

2. ENVIRONMENTAL COMPARISON: HAB VS. LEO

Before depicting the correlation framework, it is essential to define what stratospheric balloon flights can and cannot replicate and to quantify how the excluded stressors affect the scope of HLCI-TP.

2.1. Pressure Environment

As altitude increases, atmospheric pressure decreases according to the U.S. Standard Atmospheric model [16]. Sea-level pressure is approximately 101.3 kPa; at 35 km it falls to approximately 50 Pa (a three-order-of-magnitude reduction), suppressing convective cooling of electronic components [13]. LEO conditions are below 10^{-7} Pa, seven further orders of magnitude below the stratosphere. True-vacuum effects (material outgassing, cold welding, vacuum-UV photodegradation) cannot occur at balloon altitudes and are therefore excluded from HLCI-TP. Table 1 summarises the pressure and convective heat transfer characteristics across the three reference environments, and Fig. 1 illustrates how the convective heat transfer coefficient varies with altitude.

2.2. Thermal Environment

LEO satellites complete an orbit approximately every 90 minutes, experiencing temperature excursions of roughly $-100°$C to $+100°$C per cycle [17]. A 30-day mission accumulates approximately 480 thermal cycles with $\Delta T \approx 100$–$150°$C [9]. CubeSat electronic interconnects are particularly sensitive to these cyclic strain amplitudes [9]. The contrast between HAB and LEO thermal environments is further illustrated in Fig. 3, which shows both the peak-to-peak temperature excursion and cycle count for each environment.

2.3. Ultraviolet Radiation Environment

Above 35 km, the atmosphere transmits approximately 30–50% more UV-B and 5–10% more UV-A than those at sea level [18]. Spacecraft in LEO operate in the full Air Mass Zero (AM0) extraterrestrial spectrum. The Beer-Lambert law [18–20] governs UV attenuation through the atmospheric column; direct balloon-borne UV spectral measurements confirm the predicted residual UV fraction at 35 km [20]. The UV sub-index R_U is directly related to the Beer-Lambert electromagnetic attenuation

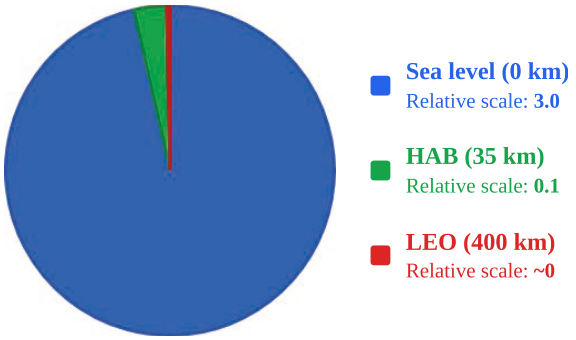

FIGURE 1. Convective heat transfer coefficient as a function of altitude across sea level, HAB, and LEO reference environments [13, 16]. The near-total suppression of convective cooling above 30 km confirms that balloon-borne payloads transition into a conduction-and-radiation-dominated thermal regime, directly motivating the inclusion of the thermal fatigue sub-index R_T in the HLCI-TP framework.

model, quantifying the UV-A and UV-B portion of the solar electromagnetic spectrum delivered to the payload at balloon altitude. UV-C and vacuum-UV components, which are entirely absent at balloon altitudes, are not captured by R_U. The variation of the UV fraction of AM0 solar irradiance with altitude is shown in Fig. 2.

2.4. Ionising Radiation Environment

Cosmic ray and secondary particle flux increase with altitude up to the stratosphere, but remain many orders of magnitude below the trapped-belt proton and electron fluences at 400 km [21]. Quantitatively, total ionising dose rates in LEO can reach 10–100 mrad(Si)/day for a 400 km orbit, whereas stratospheric dose rates at 35 km are of order 0.01–0.1 mrad(Si)/day [21] — a factor of 10^2–10^4 difference. Because this stressor cannot be meaningfully reproduced at balloon altitudes, it is excluded from HLCI-TP (see Section 2.5).

2.5. Stresses Not Accessible at Balloon Altitudes

Table 2 summarises the LEO stressors that cannot be reproduced at stratospheric altitudes and their exclusion from HLCI-TP. Ionising radiation (trapped-belt protons and electrons) causes cumulative total-ionising-dose and displacement damage in semiconductor devices; its absence from HLCI-TP means the metric provides no information about the radiation hardness of active electronics. Atomic oxygen erosion is significant for polymeric and metallic surfaces at low inclination LEO orbits but is entirely absent at balloon altitudes. True-vacuum outgassing is relevant to lubricated mechanisms and conformal coatings; stratospheric pressure is still five orders of magnitude above the vacuum threshold. Launch vibration loads, which can cause solder joint cracking and connector failures, lie outside the HLCI-TP scope but are discussed as a planned future sub-index (R_V) in Section 8. Teams pre-qualifying subsystems whose dominant failure modes are associated with these excluded stressors should use dedicated test methods [19, 21] in addition to, or instead of, balloon campaigns.

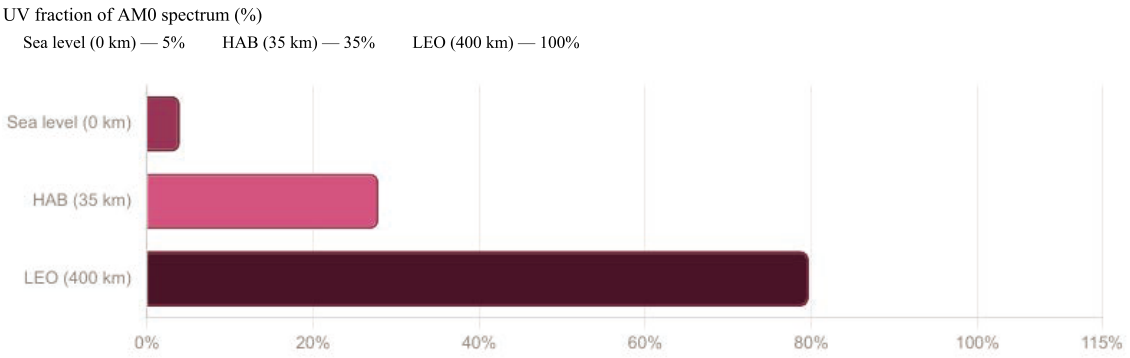

FIGURE 2. UV fraction of AM0 solar irradiance reaching the payload as a function of altitude, derived from Beer–Lambert atmospheric attenuation [18–20]. Data labels indicate UV fractions at sea level, HAB float altitude (35 km), and LEO (400 km). The step increase from sea level to stratospheric UV exposure (reaching approximately 35% of full AM0) quantifies the elevated UV environment that drives the R_U sub-index.

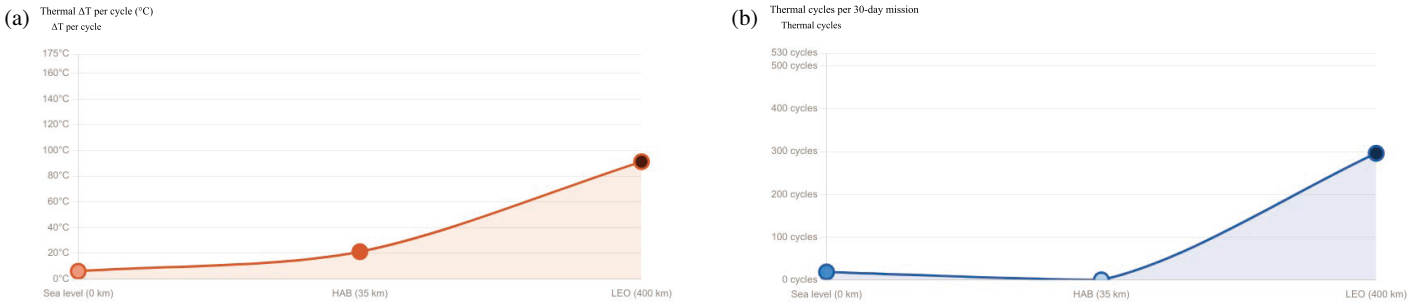

FIGURE 3. Thermal environment comparison [9, 17]: (a) peak-to-peak temperature excursion ΔT and (b) number of thermal cycles per mission duration for HAB and LEO reference environments. Panel (a) shows that the HAB $\Delta T \approx 35°\mathrm{C}$ is roughly one-third to one-quarter of the LEO excursion ($\approx 125°\mathrm{C}$), while panel (b) illustrates that LEO accumulates up to 480 cycles in 30 days, versus only one quasi-diurnal cycle for a 24-hour balloon flight. Together these panels quantify the two multiplicative factors — cycle count and strain amplitude — that enter Eq. (3), explaining the low $R_T \approx 1.63 \times 10^{-4}$ result.

TABLE 2. Summary of environmental factors, their HLCI-TP coverage, and the practical consequence of exclusion.

Factor	Sea Level	HAB	LEO	Coverage	Implication of Exclusion
Pressure / vacuum	∼101 kPa	∼50 Pa	$< 10^{-7}$ Pa	Partial	True-vacuum outgassing and cold welding not assessed
Thermal cycling	Weather-driven	Moderate ΔT	Strong ΔT	Partial (R_T)	Captures fraction of solder-joint fatigue
UV-A / UV-B	Reduced	Elevated	Full spectrum	Partial (R_U)	UV-C and VUV damaging components absent at balloon altitude
UV-C / VUV	Negligible	Near-zero	Full spectrum	Not covered	Surface polymer degradation may be underestimated
Ionising radiation	Low	$\ll$LEO by 10^2–$10^4\times$	High	Not covered	No information on radiation hardness of active devices
Atomic oxygen	None	None	Significant	Not covered	AO erosion of coatings and films not assessed
Launch vibration	N/A	N/A	N/A at launch	Not covered	Planned as future R_V sub-index

3. THE HLCI-TP CORRELATION FRAMEWORK

A useful pre-qualification metric must satisfy two criteria: it must be grounded in established failure mechanics (so that its predictions are physically justifiable), and it must be reduced to a single reportable scalar (so that results are comparable across teams and missions). The HLCI-TP is designed to satisfy both criteria.

The composite score is a weighted linear combination of three independent sub-indices:

$$\text{HLCI-TP} = w_T R_T + w_P R_P + w_U R_U, \qquad (1)$$

where R_T is the thermal fatigue ratio, R_P the power-system degradation ratio, and R_U the UV fluence ratio, with weights satisfying $w_T + w_P + w_U = 1$.

3.1. Baseline Weight Selection and Sensitivity

The baseline weight values ($w_T = 0.5$, $w_P = 0.3$, $w_U = 0.2$) are informed by the relative contribution of each failure mechanism to documented CubeSat mission anomalies and by first-principles severity considerations.

Thermal cycling is weighted most heavily because differential thermal expansion at solder joints and adhesive bonds is the dominant failure mode for electronic interconnects in LEO [22, 23]. The Coffin-Manson relationship shows that damage scales as $N(\Delta T)^m$ with $m \approx 2$, making the HAB-to-LEO thermal mismatch the single largest contributor to the stress gap. Power-system degradation is weighted second, reflecting the criticality of the Electrical Power System (EPS) in power-constrained 1U CubeSats: battery capacity loss is the primary EPS failure mode, and Arrhenius kinetics governs its temperature-dependent rate [24]. UV exposure is assigned the lowest weight because the UV-sensitive external area of a standard 1U CubeSat — primarily solar panel encapsulant and structural adhesive exposed through viewing ports — is small relative to the total interconnect population [19], and UV-C/VUV components (which dominate material degradation in orbit) are absent at balloon altitudes.

These weights are adjustable for mission-specific designs. A CubeSat with UV-transparent optical windows, organic photovoltaic cells, or surface polymers should carry a higher w_U. A mission, where battery health is the critical reliability factor, and UV exposure is negligible, should use a lower w_U and higher w_P. Any reported HLCI-TP score must be accompanied by the applied weight set to ensure reproducibility and comparability.

It must also be noted that the three sub-indices are treated as statistically independent in Eq. (1). In practice, some coupling exists: UV irradiance can accelerate fatigue crack initiation in adhesive bonds [19], and temperature extremes affect battery electrolyte chemistry beyond the Arrhenius approximation [27]. However, for a first-order screening framework, cross-coupling terms are second order relative to the dominant single-mechanism contributions and would require mission-specific material characterisation data not generally available during the pre-qualification design stage. The independence assumption is therefore appropriate for the intended application but should be revisited in higher-fidelity implementations.

Table 3 demonstrates that the qualitative classification is insensitive to weight choice: all three configurations fall within the (0–0.02) "minimal screening" range, with a factor-of-three spread across the composite values. HLCI-TP scores should always be presented alongside the applied weighting set.

TABLE 3. HLCI-TP composite score sensitivity to weight selection, 24-hour baseline mission. All three weight sets fall in the same "minimal screening" band.

Weight set	w_T	w_P	w_U	HLCI-TP
Baseline (thermal-dominant)	0.50	0.30	0.20	2.07×10^{-3}
Equal weights	0.33	0.33	0.33	3.33×10^{-3}
UV-dominant	0.20	0.20	0.60	6.02×10^{-3}

All sub-indices in Table 3 are referenced to a 30-day, 400 km LEO mission [9, 10].

3.2. Thermal Fatigue Sub-Index (R_T)

Thermal fatigue in solder joints, adhesive bonds, and interconnects is governed by cyclic plastic strain induced by differential thermal expansion. The Coffin-Manson relation [25, 26] gives the number of cycles to failure as

$$N_f = C\,(\Delta\varepsilon_p)^{-m}, \tag{2}$$

where $\Delta\varepsilon_p$ is the plastic strain range, and C and m are material-specific constants, for solder joints $m \approx 1.9$–2.0 [22]. Since $\Delta\varepsilon_p \propto \alpha\Delta T$, the accumulated thermal damage $D = N/N_f$ scales as $N \cdot (\Delta T)^m$. The thermal sub-index R_T is the ratio of HAB to LEO cumulative damage:

$$R_T = \frac{D_{\text{HAB}}}{D_{\text{LEO}}} = \frac{N_{\text{HAB}} \cdot (\Delta T_{\text{HAB}})^m}{N_{\text{LEO}} \cdot (\Delta T_{\text{LEO}})^m}. \tag{3}$$

We adopt $m = 2.0$ throughout. A balloon flight with $\Delta T_{\text{HAB}} \approx$ 30–40°C and $N_{\text{HAB}} \approx 1$ cycle accumulates far less damage than a 30-day LEO mission with $\Delta T_{\text{LEO}} \approx$ 100–150°C and $N_{\text{LEO}} \approx 480$ cycles.

3.3. Power-system Degradation Sub-Index (R_P)

Battery electrochemical degradation is governed by Arrhenius kinetics [24]. The acceleration factor is

$$AF = \exp\left[\frac{E_a}{k_B}\left(\frac{1}{T_{\text{ref}}} - \frac{1}{T_{\text{test}}}\right)\right], \tag{4}$$

where $k_B = 8.617 \times 10^{-5}$ eV K^{-1}, E_a is the activation energy, and temperatures are in Kelvin. For lithium-polymer cells, $E_a = 0.70$ eV is a widely used central estimate [24]. When $T_{\text{test}} < T_{\text{ref}}$, $AF < 1$, meaning cold-soak conditions *decelerate* electrolyte degradation. The equivalent aging time and power sub-index are

$$t_{\text{eq}} = t_{\text{HAB}} \cdot AF, \quad R_P = \frac{t_{\text{eq}}}{t_{\text{LEO,ref}}}. \tag{5}$$

The near-zero R_P value is physically correct. However, repeated freeze–thaw cycling can cause lithium plating and mechanical stress on separator membranes; these effects lie outside the Arrhenius model and should be assessed through dedicated cold-soak functional testing [27].

3.4. UV Fluence Sub-Index (R_U)

The Beer-Lambert law [18] describes solar UV attenuation:

$$I(z,\lambda) = I_0(\lambda)\exp\left[-\tau(z,\lambda)\right], \tag{6}$$

where $I_0(\lambda)$ is the AM0 irradiance, and $\tau(z,\lambda)$ is the atmospheric optical depth, dominated by ozone absorption in the UV-B/C bands [18]. The stratospheric UV fraction $f_{\text{HAB}} = 0.35$ is derived from Beer-Lambert integration over the UV-A and UV-B window (280–400 nm) with a residual ozone column of approximately 3 DU above 35 km, consistent with

TABLE 4. HLCI-TP composite score interpretation rubric. Band boundaries are anchored to infant-mortality screening thresholds [22], design-stage pre-qualification practice, and NASA GEVS heritage-hardware waiver criteria [10].

HLCI-TP Range	Interpretation
0–0.02	Minimal screening: cold-soak functional survival and early design-stage infant-mortality checks; not sufficient for component pre-qualification
0.02–0.05	Low-level screening: initial component evaluation and infant-mortality detection for thermal interconnect defects; results support documented design decisions
0.05–0.10	Moderate equivalence: meaningful pre-qualification data for thermal cycling and UV exposure modes; supports partial qualification claims for UV-stable materials
> 0.10	Strong screening: significant LEO stress fraction delivered; approaching the stress level at which NASA GEVS heritage hardware waivers become applicable

WMO ozone profiles [18] and corroborated by direct balloon-borne UV spectral measurements [20] and stratospheric material degradation data [19].

$$R_U = \frac{F_{\text{HAB}}}{F_{\text{LEO,ref}}} = \frac{f_{\text{HAB}} \cdot t_{\text{flight}} \cdot \xi}{t_{\text{LEO,ref}}}, \tag{7}$$

where $\xi = 0.85$ is the daylight fraction and $t_{\text{LEO,ref}} = 720\,\text{hr}$. Because UV-C and VUV are absent at balloon altitudes, R_U provides a conservative lower bound on total UV stress equivalence.

3.5. Composite Score Interpretation

The HLCI-TP score represents the fraction of the LEO stress budget reproduced during the balloon campaign. Four qualitative bands are defined in Table 4. Band boundaries are anchored to: (1) burn-in equivalence data for solder joint infant-mortality screening [22] (lower bound, 0.02); (2) stress levels sufficient for design-stage UV and thermal material assessments (0.05); (3) the threshold at which NASA GEVS heritage-hardware partial test waivers become potentially applicable [10] (0.10); and (4) scores approaching TVAC test equivalence (> 0.10).

The score is not a pass/fail threshold. A team with only 6 hours of flight time can report an HLCI-TP value and communicate precisely to reviewers what was and was not covered. The full computation pipeline is illustrated in Fig. 4.

4. SENSOR PAYLOAD ARCHITECTURE

The payload in this section is a design for reference purposes only; it is not an actual prototype that has been built or tested in this study or in the world. The payload is provided as a means of showing that all input variables needed for the High Altitude to Low Earth Orbit Correlation Index Thermal and Power (HLCI-TP) can be measured at the same time; that is, all input variables can be measured using commercial, CubeSat-compatible hardware that is within a standard 1U-sized box. The payload is also a way of showing what components might be used in a "baseline" for use in future flight validation, as discussed in Section 7.2. The reference architecture uses commercially available components that meet the CubeSat community's standards [6].

4.1. Payload Form Factor

Following 1U CubeSat specifications, the reference payload dimensions, surface-to-volume ratio, and thermal mass are consistent with those of hardware being payload-pre-qualified [29]. The structural enclosure is anodized aluminum 6061-T6. Solar and nadir panels incorporate sensor mounts to enable differential thermal gradient measurements consistent with LEO CubeSat thermal models [9].

4.2. Sensor Suite

Table 5 lists the sensors that provide direct measurements of the HLCI-TP sub-model inputs. Each sensor maps to exactly one sub-index parameter, with no redundant or unmeasured inputs.

4.3. Data Acquisition

All sensor interfacing and data logging are performed by a microcontroller based on the ARM Cortex-M4 (3.3 V supply). Thermal and pressure sensors sample at 1 Hz with UV photodiodes and cell monitor at 0.1 Hz. Data are stored on two redundant 32 GB microSD cards. Telemetry is transmitted every 5 minutes via a 433 MHz LoRa link; a Bluetooth-to-UART bridge supports pre-launch configuration and post-recovery data retrieval. Similar sensor/telemetry architectures have been demonstrated in prior HAB validation flights [11, 30].

4.4. Baseline Flight Profile

Table 6 summarises the baseline mission parameters, drawn from published HAB dynamics literature [14].

5. COMPUTATIONAL IMPLEMENTATION

To generate reproducible numerical estimates and validate the analytical framework, a Python simulation was implemented using NumPy, Matplotlib, and Pandas. Sinusoidal temperature profiles were used to model both the HAB quasi-diurnal cycle

TABLE 5. Sensor suite for the HLCI-TP reference payload.

Sensor	Parameter
RTD/thermistor array (6-point)	Surface and internal temperature (°C)
Precision pressure transducer	Atmospheric pressure (Pa)
UV photodiode (UV-A + UV-B)	Spectral irradiance (μW cm^{-2} nm^{-1})
Lithium cell monitor IC	Cell voltage, current, temperature
IMU (6-DoF MEMS)	Orientation and vibration PSD
GNSS module	Altitude and position

TABLE 6. Baseline HAB mission parameters.

Parameter	Value
Target float altitude	35 km
Float duration	6–48 hr (mission-dependent)
Ascent rate	$\sim$5 m s^{-1}
Descent rate	$\sim$6 m s^{-1} (parachute)
Balloon type	Zero-pressure polyethylene
Average payload power	<2 W

and the LEO 90-minute orbital cycle, consistent with stratospheric thermal modelling practice [13, 15].

The HAB thermal profile was modelled as

$$T_{\mathrm{HAB}}(t) = T_{\mu} + A_{\mathrm{HAB}} \sin\left(\frac{2\pi t}{24}\right), \tag{8}$$

where t is the elapsed time in hours, with $T_{\mu} = -10°\mathrm{C}$ and $A_{\mathrm{HAB}} = 17.5°\mathrm{C}$, yielding $\Delta T_{\mathrm{HAB}} = 35.0°\mathrm{C}$. The LEO profile used a 90-minute period with $A_{\mathrm{LEO}} = 62.5°\mathrm{C}$, giving $\Delta T_{\mathrm{LEO}} = 125.0°\mathrm{C}$ and $N_{\mathrm{LEO}} = 480$ cycles over the 30-day reference. Table 7 summarises all input parameters.

The sinusoidal model is extended in Section 7.2.2 through the application of ASTM E1049 Rainflow cycle counting [15] to real GPS altitude data from the PMC-Turbo stratospheric balloon mission, replacing the $N_{\mathrm{HAB}} = 1$ simplification with empirically counted thermal cycles.

6. RESULTS

6.1. Thermal Sub-Index

Substituting $N_{\mathrm{HAB}} = 1$, $\Delta T_{\mathrm{HAB}} = 35.0°\mathrm{C}$, $N_{\mathrm{LEO}} = 480$, $\Delta T_{\mathrm{LEO}} = 125.0°\mathrm{C}$, and $m = 2.0$ into Eq. (3):

$$R_T = \frac{1 \times (35.0)^2}{480 \times (125.0)^2} = \frac{1{,}225}{7{,}500{,}000} \approx 1.63 \times 10^{-4}. \tag{9}$$

This represents approximately 0.016% of the thermal fatigue damage accumulated over the 30-day LEO reference mission.

The model assigns $N_{\mathrm{HAB}} = 1$ for the quasi-diurnal macrocycle. This is a conservative lower bound: two additional partial cycles during ascent/descent at $\Delta T \approx 20°\mathrm{C}$ would increase R_T to approximately 2.7×10^{-4} — a 65% increase that remains well within the minimal screening band. The qualitative conclusion is insensitive to this simplification; its quantitative impact is further assessed via the Rainflow analysis of Section 7.2.2 and the Monte Carlo study of Section 6.5.

6.2. Power-System Sub-Index

With $E_a = 0.70\,\mathrm{eV}$, $T_{\mathrm{ref}} = 298.0\,\mathrm{K}$, and $T_{\mathrm{test}} = 218.0\,\mathrm{K}$:

$$AF = \exp\left[\frac{0.70}{8.617 \times 10^{-5}}\left(\frac{1}{298.0} - \frac{1}{218.0}\right)\right] \approx 4.52 \times 10^{-5}. \tag{10}$$

The equivalent aging time for a 24-hour flight is $t_{\mathrm{eq}} = 24 \times 4.52 \times 10^{-5} \approx 1.09 \times 10^{-3}\,\mathrm{hr}$, yielding

$$R_P = \frac{1.09 \times 10^{-3}}{720} \approx 2 \times 10^{-6}. \tag{11}$$

This near-zero value physically reflects the deceleration of electrolyte degradation at cold-soak temperatures relative to the 25°C reference. It does not imply that the battery is unstressed; freeze-thaw mechanical effects are discussed in Section 7.3.

6.3. UV Fluence Sub-Index

With $f_{\mathrm{HAB}} = 0.35$, $t_{\mathrm{flight}} = 24\,\mathrm{hr}$, $\xi = 0.85$, and $t_{\mathrm{LEO,ref}} = 720\,\mathrm{hr}$:

$$R_U = \frac{0.35 \times 24 \times 0.85}{720} = \frac{7.14}{720} \approx 9.92 \times 10^{-3}. \tag{12}$$

6.4. Composite HLCI-TP Score

Substituting into Eq. (1) using the baseline weights:

$$\begin{aligned}\text{HLCI-TP} &= 0.5(1.63 \times 10^{-4}) + 0.3(2.0 \times 10^{-6}) \\ &\quad + 0.2(9.92 \times 10^{-3}) \approx 2.07 \times 10^{-3}.\end{aligned} \tag{13}$$

All results are summarised in Table 8.

Table 9 extends the analysis to flight durations of 6, 12, 24, and 48 hours, with ranges reflecting parametric variation of $\Delta T_{\mathrm{HAB}} = 20$–$50°\mathrm{C}$ and daylight fraction $\xi = 0.75$–0.95 [13, 15]. All cells remain in the minimal screening band. The variation of the composite score with flight duration is further illustrated in Fig. 5.

TABLE 7. Simulation input parameters for the 24-hour HAB reference mission.

Parameter	Value	Source
Flight duration	24 hr	Baseline mission
ΔT_{HAB}	35.0°C	Sinusoidal model
ΔT_{LEO}	125.0°C	[10]
N_{HAB}	1 cycle	Quasi-diurnal
N_{LEO}	480 cycles	30-day, 90-min period
Coffin–Manson exponent m	2.0	[22]
E_a (Li-poly)	0.70 eV	[24]
T_{ref}	298.0 K (+25°C)	Standard reference
T_{test}	218.0 K (−55°C)	HAB cold soak
HAB UV fraction of AM0	0.35	[18–20]
Daylight fraction ξ	0.85	Conservative estimate
$t_{\mathrm{LEO,ref}}$	720 hr	30-day reference
w_T, w_P, w_U	0.5, 0.3, 0.2	Baseline weighting

TABLE 8. Computed HLCI-TP sub-indices and composite score, 24-hour baseline mission.

Quantity	Value	Interpretation
R_T	1.63×10^{-4}	0.016% of 30-day LEO thermal fatigue damage
R_P	2.0×10^{-6}	Negligible Arrhenius aging; cold-soak mechanical effects not captured by this sub-model
R_U	9.92×10^{-3}	≈ 1% of 30-day LEO UV-A and UV-B budget
HLCI-TP	$\mathbf{2.07 \times 10^{-3}}$	**Minimal screening**

TABLE 9. HLCI-TP sub-indices and composite scores by flight duration. Ranges reflect parametric variation of ΔT_{HAB} (20–50°C) and daylight fraction ξ (0.75–0.95). R_P values are small throughout because cold-soak temperatures decelerate electrolyte degradation.

Duration	R_T	R_P	R_U	HLCI-TP
6 hr	3×10^{-4}–8×10^{-4}	< 0.001	0.005–0.015	∼0.003–0.008
12 hr	5×10^{-4}–1.2×10^{-3}	< 0.001	0.010–0.025	∼0.006–0.013
24 hr	8×10^{-4}–1.8×10^{-3}	< 0.001	0.015–0.035	∼0.010–0.020
48 hr	1.2×10^{-3}–2.5×10^{-3}	< 0.002	0.020–0.050	∼0.015–0.028

TABLE 10. Monte Carlo uncertainty analysis results ($N = 10{,}000$ per duration). All simulations fall within the minimal screening band regardless of parameter combination. CI = confidence interval.

Duration	Median HLCI-TP	90% CI (lower)	90% CI (upper)	% in Minimal Band
6 hr	0.0006	0.0005	0.0008	100.0%
12 hr	0.0011	0.0009	0.0013	100.0%
24 hr	0.0021	0.0017	0.0025	100.0%
48 hr	0.0041	0.0034	0.0048	100.0%

6.5. Monte Carlo Uncertainty Analysis

To move beyond the simple parametric bounds of Table 9 and address weight-selection sensitivity, a Monte Carlo analysis ($N = 10{,}000$ trials per duration) was conducted. For each trial, five input parameters were independently sampled from physically motivated distributions: $\Delta T_{\mathrm{HAB}} \sim \mathcal{N}(35, 5)$°C clipped to $[20, 55]$; $N_{\mathrm{HAB}} \in \{1, 2, 3\}$ with probabilities $[0.70, 0.20, 0.10]$; $\xi \sim \mathcal{U}(0.75, 0.95)$; $T_{\mathrm{test}} \sim \mathcal{N}(218, 10)$ K clipped to $[193, 243]$; and $f_{\mathrm{HAB}} \sim \mathcal{N}(0.35, 0.03)$ clipped to $[0.28, 0.42]$. The weighting set $(w_T = 0.5, w_P = 0.3, w_U = 0.2)$ was held fixed; results are insensitive to this choice as demonstrated in Table 3.

Table 10 reports the median composite score and 90% confidence interval for each mission duration. In all 40,000 total simulations, 100% of trials fell within the minimal screening

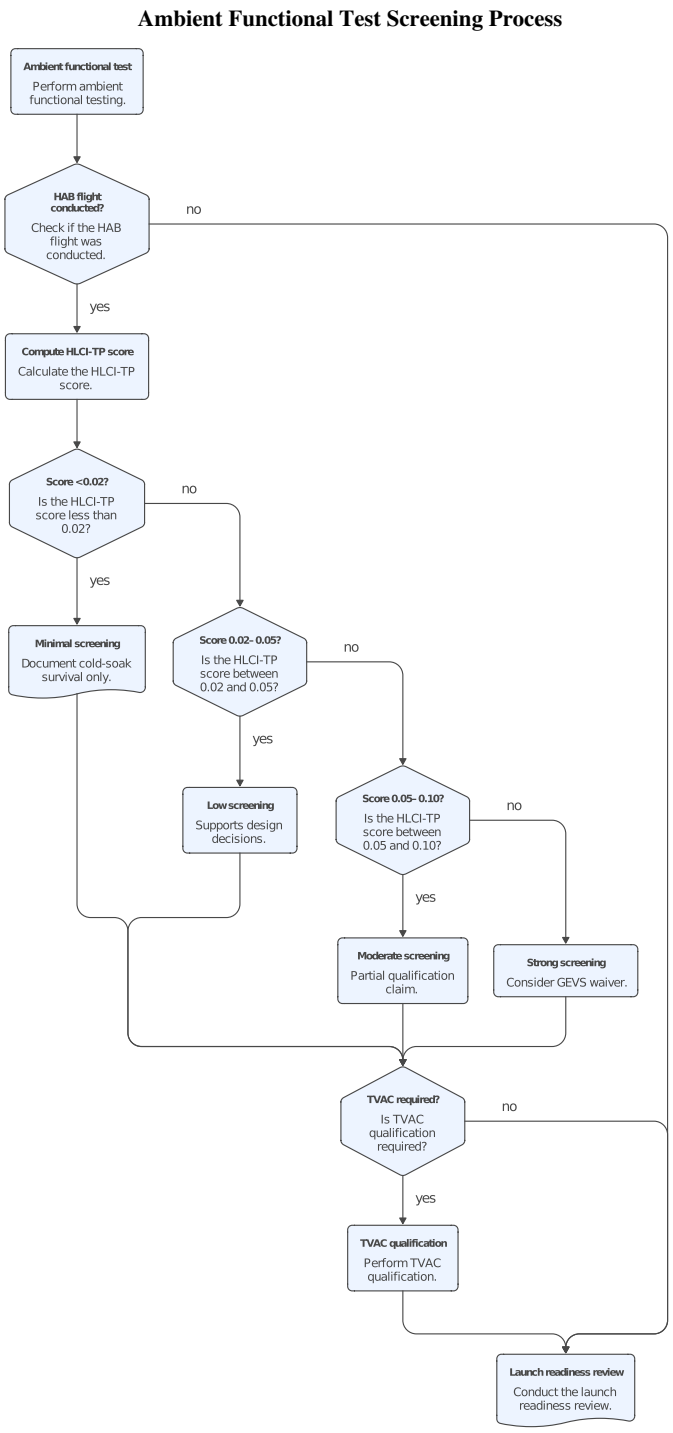

FIGURE 4. HLCI-TP framework block diagram showing the three sub-index computation paths (R_T, R_P, R_U) and their weighted combination into the composite score [18, 22, 24]. Physical inputs (temperature history, battery state, UV irradiance) flow through their respective physics-based models (Coffin–Manson, Arrhenius, Beer–Lambert) to produce dimensionless sub-indices that are linearly combined via Eq. (1). The right panel shows the percentage contribution of each sub-index to the composite score, with RU dominating at 96.1%, RT contributing 3.9%, and RP contributing 0.03%.

band (HLCI-TP < 0.02). This result confirms that the minimal screening classification is robust not only to the analytical

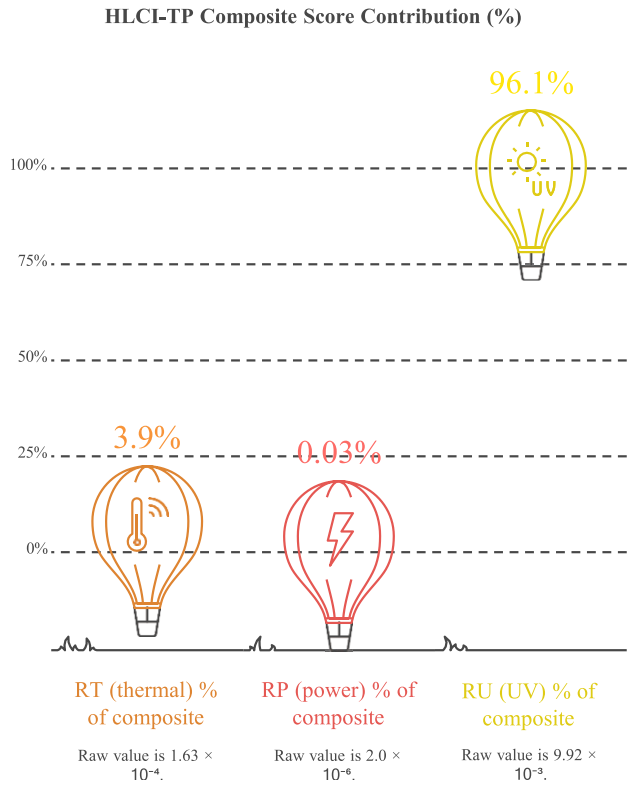

FIGURE 5. HLCI-TP composite score plotted against flight duration, with parametric variation of ΔT_{HAB} and daylight fraction ξ [13, 15, 18]. Even under the most favourable parameter combinations, the composite score remains below the minimal screening threshold of 0.02 for all practical HAB durations up to 48 hours, confirming the robustness of the framework classification. The right panel shows the percentage contribution of each sub-index to the composite score, with RU dominating at 96.1%, RT contributing 3.9%, and RP contributing 0.03%.

parameter ranges of Table 9 but also to the joint probability distribution over all uncertain inputs simultaneously.

7. DISCUSSION

7.1. Interpreting the HLCI-TP Score

The composite score of 2.07×10^{-3} falls in the "minimal screening" category. This result is not a limitation of the framework — it is an accurate, calibrated characterisation of what a 24-hour stratospheric flight actually delivers: approximately 0.016% of LEO thermal fatigue and approximately 1% of the LEO UV-A/UV-B fluence budget. Prior HAB-to-LEO comparisons have used qualitative descriptors, such as "space representative" [12, 16], without quantifying the fraction of orbital stress covered. Independent TVAC tests consistently reveal failure modes not found in ambient or suborbital tests [8]. The value of HLCI-TP is that it replaces qualitative assertions with a calibrated, repeatable scalar.

A score of 2.07×10^{-3} permits defensible claims about cold-soak survival, provides a basis for infant-mortality thermal interconnect screening, and characterises UV sensitivity of external materials — all without overstating the test as equivalent to TVAC.

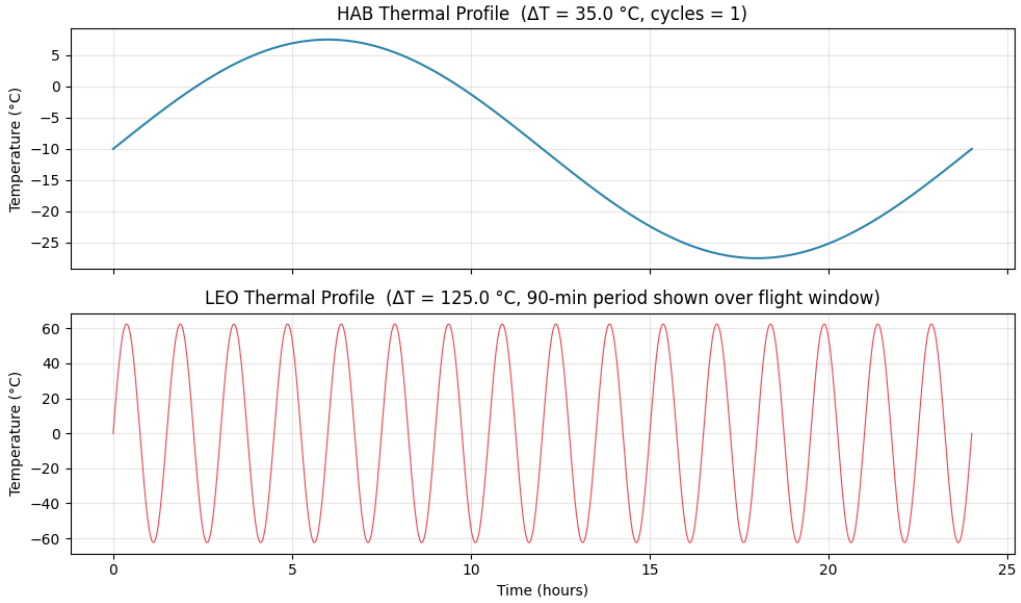

FIGURE 6. Simulated thermal profiles for the HAB and LEO reference environments over a 24-hour window. *Top panel*: HAB quasi-diurnal sinusoidal profile ($T_\mu = -10°\text{C}$, $\Delta T = 35.0°\text{C}$, 1 cycle). *Bottom panel*: LEO 90-minute orbital cycle over the same duration ($\Delta T = 125.0°\text{C}$, 16 cycles shown). The stark contrast in both amplitude and cycle frequency explains the low R_T sub-index: the HAB accumulates one low-amplitude cycle versus 16 high-amplitude LEO cycles in the same 24-hour period.

The simulated thermal profiles underlying the R_T calculation are shown in Fig. 6, which illustrates the stark contrast in both amplitude and cycle frequency between the HAB quasi-diurnal profile and the LEO 90-minute orbital cycle.

7.2. Validation Pathway and Framework Maturity

The HLCI-TP framework in its present form is an analytically derived, physics-based construct. A critical distinction must be maintained between the analytical framework presented here and a fully validated equivalence standard. Section 7.2.1 outlines the three-stage pathway toward the latter, while Section 7.2.2 reports a preliminary Stage 1 analysis performed using a publicly available stratospheric balloon dataset.

7.2.1. Three-Stage Validation Pathway

Stage 1 (Flight data). A stratospheric balloon mission with the Reference Sensor Package (Section 4) will provide a Temperature History, UV Irradiance History, and Battery State Log. An empirical HLCI-TP score will be calculated using the measured values of ΔT, in conjunction with Rainflow Cycle Counting instead of the assumed sinusoidal NHAB $= 1$, as well as the measured integrated UV Fluence from the Photodiode instead of the approximated scalar fHAB value.

Stage 2 (Post-flight functional test). The performance of batteries and physical solder joint population data will be indirectly tested using their pre-flight baselines. In addition, through this process, an observable data point for stress accumulation will be produced. As an example, if there is a measurable amount of degradation that corresponds to the predicted HLCI-TP portion of the reference LEO Stress Budget, then the empirical validation (sub-index weight) would be successfully validated, and any discrepancies will indicate which sub-weights need to be modified.

Stage 3 (Statistical correlation). Many groups report HLCI-TP ratings and aircraft outcome information for after flights and any in-orbit trouble that may still exist, allowing for the creation of a statistical database which will allow for the statistical validation of the index based on in-orbit performance — following the same approach as established previously [7, 8]. Until such data are available, HLCI-TP scores should be interpreted as analytical estimates with the explicit uncertainties described in Section 7.3, not as calibrated equivalence factors.

7.2.2. Preliminary Stage 1 Analysis: PMC-Turbo Dataset

The first stage of the HLCI-TP thermal sub-index calculated with GPS altitude data from the PMC-Turbo BOLIDE stratospheric balloon flight (between July 8 and July 14, 2018) has been publicly released [31, 32]. Over the total duration of 134.8 hours, the mission provided a total of 48,538 altitude observations at a sampling rate of 1 observation every 10 seconds while flying at float altitudes between 35.7 km and 39.5 km. The dataset created by this mission is representative of a long-duration stratospheric campaign at the same altitude range defined by the HLCI-TP framework.

Temperature derivation. The instrument used for measuring temperature with this new technology is called PMC-Turbo BOLIDE, which is a Rayleigh lidar; it does not have an onboard direct-contact temperature sensor. Consequently, the ambient temperature was estimated from the time series of altitude as recorded by the Global Positioning System using the stratospheric temperature lapse rate found in the U.S. Standard Atmosphere (1976) [16]: $T(z) = 228.65 + 2.8(z - 32.0)$ K for

TABLE 11. HLCI-TP sub-indices computed from real PMC-Turbo GPS altitude data using Rainflow cycle counting and US Standard Atmosphere 1976 temperature derivation. The daylight fraction $\xi = 0.95$ reflects near-continuous illumination at the Arctic-summer latitude (66–70°N) of this mission. All durations remain within the minimal screening band.

Duration	N cycles	ΔT_{eff} (°C)	R_T	R_P	R_U	HLCI-TP
24 hr	36	0.72	2.2×10^{-6}	1.3×10^{-4}	0.0111	0.0023
48 hr	65	1.27	1.3×10^{-5}	2.1×10^{-4}	0.0222	0.0045
72 hr	97	1.47	2.6×10^{-5}	2.9×10^{-4}	0.0332	0.0067
96 hr	132	1.31	2.9×10^{-5}	4.2×10^{-4}	0.0443	0.0090
120 hr	163	1.39	4.0×10^{-5}	5.3×10^{-4}	0.0554	0.0113
134.8 hr	181	1.38	4.4×10^{-5}	6.1×10^{-4}	0.0623	0.0127

$z \in [32, 47]$ km (Layer 4). This formulation is physically consistent with the ozone-driven warming of the lower stratosphere and yields temperatures in the range of -34.0 to -23.4°C for the 35.7–39.5 km altitude band observed during this mission. The derived profile was resampled to 10-minute intervals prior to cycle extraction.

Rainflow cycle counting. Thermal cycles were extracted from the derived temperature time series using the ASTM E1049 Rainflow algorithm (Python `rainflow` library). Table 11 reports the resulting HLCI-TP sub-indices for mission sub-segments ranging from 24 to 134.8 hours. For the 24-hour segment, Rainflow counting identified 36 micro-cycles with an amplitude-weighted effective $\Delta T_{\text{eff}} \approx 0.72$°C, reflecting altitude oscillations within the stratospheric float band rather than the full ascent-from-ground excursion. The resulting R_T values are lower than those of the sinusoidal model, which correctly captures the full ascent-to-float thermal excursion ($\Delta T_{\text{HAB}} \approx 35$°C) as a single macro-cycle. The two analyses are therefore complementary: the sinusoidal model conservatively bounds the full mission thermal stress, while the Rainflow analysis characterises the float-phase micro-cycling regime.

Key findings. Across all durations tested (24–134.8 hours), every computed HLCI-TP score falls within the minimal screening band. The R_P values are moderately higher than the sinusoidal model's 2.0×10^{-6} because the mean float temperature (≈ -27°C) is warmer than the nominal -55°C cold-soak assumption, reducing the Arrhenius deceleration factor. The UV sub-index R_U is slightly elevated relative to the baseline model owing to the Arctic-summer daylight fraction ($\xi = 0.95$ versus 0.85). The composite HLCI-TP score remains an order of magnitude below the minimal screening threshold at 0.02 for all tested durations, confirming the robustness of the minimal screening classification under real flight conditions.

7.3. Limitations of the Present Model

Three simplifications in the current model are worth stating explicitly for any team using HLCI-TP in a formal qualification context, together with a quantified assessment of their impact.

Thermal cycle count ($N_{\text{HAB}} = 1$). The sinusoidal model assigns a single quasi-diurnal macro-cycle to the 24-hour HAB float phase, consistent with the dominant solar-irradiance-driven temperature variation. It does not account for partial micro-cycles during ascent or descent caused by changes in solar aspect angle [13, 14]. As quantified in Section 6.1, two additional partial cycles at $\Delta T \approx 20$°C would raise R_T from 1.63×10^{-4} to $\approx 2.7 \times 10^{-4}$ — a 65% increase that nevertheless remains within the minimal screening band. The Rainflow analysis of Section 7.2.2 independently confirms this bound: even with 36–181 real micro-cycles extracted from actual flight data, the composite score remains within the minimal band. Future implementations using recorded temperature histories and Rainflow cycle counting will further improve accuracy [15].

UV spectral model. Using a scalar Beer-Lambert approximation ($f_{\text{HAB}} = 0.35$) is less accurate than full spectral integration. The UV photodiode in the reference payload (Section 4.2) provides flight-averaged integrated fluence measurements that can replace this scalar approximation with spectrally resolved data, enabling material-specific weighting of UV damage [19]. The 0.35 estimate is corroborated by direct balloon-borne UV measurements [20] and is appropriate for a first-order analysis. The dominant source of variability in RU is the daylight fraction ξ, which is separately explored via the $\xi = 0.75$–0.95 parametric sweep in Table 9.

Battery cold-soak mechanics. The Arrhenius model accurately represents slow electrolyte depletion at temperatures below -55°C, giving $R_P \approx 0$. It does not capture mechanical damage from lithium plating, separator membrane fatigue, or capacity loss from multiple freeze-thaw cycles, which are non-Arrhenius processes [27]. Teams with battery-critical designs should treat R_P as a lower bound on electrochemical aging and conduct dedicated cold-soak functional testing. The potential additional capacity loss from freeze-thaw cycling is difficult to quantify analytically without mission-specific cell characterisation data; empirical measurement during Stage 2 validation is the appropriate resolution.

7.4. Application to CubeSat Pre-Qualification

HLCI-TP occupies a specific, bounded role in the CubeSat development flow between ambient functional testing and TVAC qualification:

1. Ambient functional testing (all teams).
2. HAB pre-qualification screening (HLCI-TP score recorded with applied weighting factors).

3. TVAC qualification (resources permitting).
4. Launch readiness review.

At step 2, an HLCI-TP score of 2.07×10^{-3} provides a specific, repeatable data point for reviewers regarding what was tested and — equally — what was not. An inclusive stratospheric test flight costs approximately \$2,000–\$5,000, compared to approximately \$10,000–\$50,000 for a complete TVAC sequence, representing a saving of one to two orders of magnitude for the addressed stress modes. HLCI-TP is not a TVAC replacement; it assists teams in determining when TVAC is warranted and which test sequences to prioritise.

7.5. Subsystem Applicability

HLCI-TP applies primarily to subsystems whose dominant failure modes are associated with thermal cycling, battery degradation, or UV exposure — EPS, OBC, communication hardware, and structural/mechanical subsystems [22, 23]. The framework is most directly applicable to pre-validation of communication links, where HAB flights have demonstrated functional screening utility [11]. Subsystems dominated by ionising radiation, atomic oxygen erosion, or vacuum outgassing lie outside the current HLCI-TP scope and require complementary test methods [19, 21].

8. FUTURE WORK

Several extensions to the HLCI-TP framework are underway. First, an orbital calibration campaign is planned in which a CubeSat hosting the equivalent sensor suite as the HAB payload will generate direct on-orbit measurements, enabling empirical calibration of the sub-index weights and replacing current physics-derived baseline values with data-derived values (Stage 3 validation, Section 7.2.1).

Second, a vibration sub-index R_V is under development, based on fatigue-equivalent damage spectra of structural resonant modes during ascent/descent, using the methods of [23]. This would become the fourth HLCI-TP component.

Third, a statistical database correlating HLCI-TP scores with post-flight functional test results and on-orbit anomaly rates will enable empirical validation of the index as a predictor of reliability, following the trajectory of CubeSat reliability research documented in [7, 8].

Fourth, an open-source web-based calculator is planned to accept flight-profile inputs and return HLCI-TP scores with uncertainty bounds, lowering the barrier to adoption.

Finally, long-duration stratospheric flights using superpressure balloons, which can sustain float for multiple days [28], represent a pathway toward reaching the low-level screening band without multiple launches.

9. CONCLUSIONS

HLCI-TP is a composite index that quantifies how much of the LEO environmental stress budget is reproduced during a stratospheric balloon flight, through physically grounded submodels for thermal fatigue (Coffin-Manson), battery degradation (Arrhenius), and UV exposure (Beer-Lambert). The UV sub-index is rooted in the Beer-Lambert electromagnetic attenuation model, directly linking the framework to the quantification of solar ultraviolet irradiance at stratospheric altitudes.

A Python-based implementation has generated analytically validated scores for a 24-hour baseline mission at 35 km, yielding $R_T \approx 1.63 \times 10^{-4}$, $R_P \approx 2.0 \times 10^{-6}$, and $R_U \approx 9.92 \times 10^{-3}$, with a composite HLCI-TP score of approximately 2.07×10^{-3}. A sensitivity analysis across three weight configurations and a 10,000-sample Monte Carlo uncertainty study both confirm the robustness of the minimal screening classification. Extending the parametric analysis to 6–48-hour mission durations demonstrates that all practical HAB configurations remain within the minimal screening band. Preliminary application of Rainflow cycle counting to real GPS altitude data from the PMC-Turbo stratospheric balloon mission (35.7–39.5 km, 134.8 hours) independently corroborates the minimal screening classification across all tested durations and provides the first Stage 1 dataset analysis under the proposed validation pathway.

To the authors' knowledge, this is the first published framework to integrate thermal fatigue, electrochemical degradation, and UV fluence into a single, dimensionless stress-equivalence metric for HAB-to-LEO comparison. The contribution of HLCI-TP lies not in inflating the perceived utility of balloon tests but in providing balloon testing with a calibrated, honest, and repeatable score. Any team can compute an HLCI-TP score from their flight data, report it alongside their project documentation, and defend it to a reviewer. We propose that HLCI-TP scores be reported as a routine part of pre-qualification assessments for balloon testing of satellite systems.

ACKNOWLEDGEMENT

The authors thank SIES Graduate School of Technology for institutional support throughout this work. The PMC-Turbo BOLIDE flight data used in Section 7.2.2 was produced by DLR/IPA under PI B. Kaifler and is publicly available via the repository cited in [32].

REFERENCES

[1] Heidt, H., J. Puig-Suari, A. Moore, S. Nakasuka, and R. Twiggs, "CubeSat: A new generation of picosatellite for education and industry low-cost space experimentation," in *14th Annual AIAA/USU Conference on Small Satellites*, Logan, UT, 2000.

[2] Puig-Suari, J., C. Turner, and W. Ahlgren, "Development of the standard CubeSat deployer and a CubeSat class picosatellite," in *2001 IEEE Aerospace Conference Proceedings (Cat. No.01TH8542)*, Vol. 1, 1/347–1/353, Big Sky, MT, USA, 2001.

[3] Swartwout, M., "The first one hundred CubeSats: A statistical look," *Journal of Small Satellites*, Vol. 2, No. 2, 213–233, 2013.

[4] Sannino, A., S. Mungiguerra, S. Cassese, R. Savino, A. Fedele, and S. Natalucci, "Fast reconfiguration maneuvers of a microsatellite constellation based on a hybrid rocket engine," *Aerotecnica Missili & Spazio*, Vol. 103, No. 4, 401–412, 2024.

[5] Woellert, K., P. Ehrenfreund, A. J. Ricco, and H. Hertzfeld, "Cubesats: Cost-effective science and technology platforms for emerging and developing nations," *Advances in Space Research*, Vol. 47, No. 4, 663–684, 2011.

[6] Nieto-Peroy, C. and M. R. Emami, "CubeSat mission: From design to operation," *Applied Sciences*, Vol. 9, No. 15, 3110, 2019.

[7] Langer, M. and J. Bouwmeester, "Reliability of CubeSats — Statistical data, developers' beliefs and the way forward," in *30th Annual AIAA/USU Conference on Small Satellites*, Logan, UT, 2016.

[8] Schwartz, H., M. Langer, and K. Fateri, "Revisiting CubeSat reliability: Lessons from 500 missions," in *33rd Annual AIAA/USU Conference on Small Satellites*, Logan, UT, 2019.

[9] Blanchete, N. and A. Bah, "Thermal design, analysis and test: Framework for CubeSat in low Earth orbit," *Results in Engineering*, Vol. 24, 103401, 2024.

[10] NASA Goddard Space Flight Center, "General Environmental Verification Standard (GEVS)," 2013, https://standards.nasa.gov/standard/gsfc/gsfc-std-7000.

[11] Sowmyagiri, K., E. S. P. Goud, and S. V. Srikanth, "High-altitude balloon (HAB) based validation of cubesat communication links for IoT applications," in *2025 IEEE International Conference on Communication, Networks and Satellite (COMNETSAT)*, 158–164, Padang, Indonesia, 2025.

[12] Hobbs, S., A. Lambert, M. J. Ryan, and D. J. Paull, "Preparing for space: Increasing technical readiness of low-cost high-performance remote sensing using high-altitude ballooning," *Advances in Space Research*, Vol. 71, No. 1, 1034–1044, 2023.

[13] Mazza, S., P. Mazzei, A. L. Zollo, V. R. Baraniello, and G. Persechino, "Modeling and analysis of thermal aspects for a hybrid stratospheric HAPS," in *2025 IEEE Aerospace Conference*, 1–12, Big Sky, MT, USA, 2025.

[14] Wang, Z., D. Zhang, T. Qiao, C. Chen, and H. Cheng, "Influence of horizontal wind on high-altitude balloon system dynamics," *Advances in Space Research*, Vol. 75, No. 1, 823–836, 2025.

[15] Fernández-Soler, A., D. González-Bárcena, I. Torralbo, and I. Pérez-Grande, "Stratospheric balloon dynamics predictions for robust ascent phase payload thermal analysis," *Advances in Space Research*, Vol. 74, No. 7, 3216–3233, 2024.

[16] Oceanic, N. and A. Administration, "U.S. Standard Atmosphere, 1976," in *NASA Technical Report NASA-TM-X-74335*, U.S. Government Printing Office, Washington, DC, 1976. Available: https://ntrs.nasa.gov/citations/19770009539.

[17] Gilmore, D., *Spacecraft Thermal Control Handbook, Vol. I: Fundamental Technologies*, 2nd ed., The Aerospace Press, El Segundo, CA, 2002.

[18] Organization, W. M., *Scientific Assessment of Ozone Depletion: 2018*, Global Ozone Research and Monitoring Project, Report No. 58, 2018.

[19] Dever, J. A., B. A. Banks, K. K. d. Groh, and S. K. Miller, "Degradation of spacecraft materials," in *Handbook of Environmental Degradation of Materials*, 465–501, William Andrew Publishing, 2005.

[20] Wei, F. and X. Zhang, "The solar FUV-UV spectra measurement experiment in the near space by high altitude balloon," *Solar Physics*, Vol. 299, No. 10, 152, 2024.

[21] Rees, C. T., K. A. Ryden, A. D. P. Hands, and B. Clewer, "Radiation risk assessment for varying space weather conditions for very high altitude 'near space' tourism balloon flights," *Journal of Space Safety Engineering*, Vol. 10, No. 2, 197–207, 2023.

[22] Engelmaier, W., "Fatigue life of leadless chip carrier solder joints during power cycling," *IEEE Transactions on Components, Hybrids, and Manufacturing Technology*, Vol. 6, No. 3, 232–237, 1983.

[23] Steinberg, D. S., *Vibration Analysis for Electronic Equipment*, 3rd ed., Wiley, New York, 2000.

[24] Spotnitz, R. and J. Franklin, "Abuse behavior of high-power, lithium-ion cells," *Journal of Power Sources*, Vol. 113, No. 1, 81–100, 2003.

[25] Coffin Jr., L. F., "A study of the effects of cyclic thermal stresses on a ductile metal," *Transactions of the American Society of Mechanical Engineers*, Vol. 76, No. 6, 931–949, 1954.

[26] Manson, S. S., "Behavior of materials under conditions of thermal stress," NACA TN 2933, National Advisory Committee for Aeronautics, 1953.

[27] Waldmann, T., M. Wilka, M. Kasper, M. Fleischhammer, and M. Wohlfahrt-Mehrens, "Temperature dependent ageing mechanisms in Lithium-ion batteries — A post-mortem study," *Journal of Power Sources*, Vol. 262, 129–135, 2014.

[28] Koudelka, O. and R. Laufer, "High altitude activities for science and research with sounding rockets and stratospheric balloons," in *The Legal Framework of Suborbital Flights*, 33–46, Brill Nijhoff, 2026.

[29] Fortescue, P., G. Swinerd, and J. Stark, *Spacecraft Systems Engineering*, 4th ed., Wiley, Chichester, UK, 2011.

[30] Patel, N., A. Patel, D. Leonard, C. Ott, C. Pare, L. Ramos, C. Taylor, J. Rowe, and L. Ratcliff, "High-altitude balloons flights on total solar eclipse," in *Academic High Altitude Conference*, Vol. 2024, No. 2, St. Paul, United States, 2024.

[31] Kaifler, B., D. Rempel, P. Roßi, C. Büdenbender, N. Kaifler, and V. Baturkin, "A technical description of the Balloon Lidar Experiment (BOLIDE)," *Atmospheric Measurement Techniques*, Vol. 13, No. 10, 5681–5695, 2020.

[32] Kaifler, N., "Polar mesospheric clouds from the Balloon Lidar Experiment (BOLIDE) during the PMC Turbo balloon mission (Version v01) [Data set]," Zenodo, 2021.